

# Constraints on SMEFT operators from $Z \rightarrow \mu\mu b\bar{b}$ decay

Zijian Wang,\* Tianyi Yang, Tianyu Mu, Andrew Levin, and Qiang Li

School of Physics and State Key Laboratory of Nuclear Physics and Technology, Peking University, Beijing, 100871, China

(Dated: December 30, 2025)

The Standard Model Effective Field Theory (SMEFT) provides a systematic framework to probe indirect effects of heavy new physics via precision measurements. While SMEFT constraints have been extensively studied using purely leptonic  $Z$  decays and inclusive  $Z$  production, mixed leptonic–hadronic modes remain largely unexplored. In this work, we analyze  $Z \rightarrow \mu\mu b\bar{b}$  decays within the SMEFT framework, deriving constraints on dimension-six operators that affect four-fermion interactions between leptons and bottom quarks, as well as  $Z$ –fermion couplings. Signal and background events are simulated with state-of-the-art Monte Carlo tools, including detector effects such as  $b$ -tagging, and limits on the relevant Wilson coefficients are extracted using kinematic distributions and a profile likelihood approach. Our results provide complementary constraints to existing SMEFT studies and yield the first process-specific limits on flavor-resolved four-fermion operators involving muons and bottom quarks from  $Z$  decays.

## I. INTRODUCTION

The  $Z$  boson has long served as a cornerstone of precision tests of the electroweak sector of the Standard Model (SM). At both the LEP and the LHC, measurements of  $Z$ -boson production and decay have reached a precision that allows indirect probes of physics beyond the SM [1–3]. In particular, rare and multi-body  $Z$ -boson decays probe kinematic regimes and operator structures not fully constrained by inclusive observables.

The Standard Model Effective Field Theory (SMEFT) offers a model-independent framework to parameterize the effects of heavy new physics through higher-dimensional operators constructed from SM fields [4–6]. In recent years, SMEFT interpretations of  $Z$ -boson observables have attracted considerable attention. Purely leptonic decay modes, such as  $Z \rightarrow 4\ell$ , provide stringent constraints on electroweak and four-lepton operators, while complementary information has been obtained from SMEFT analyses of inclusive  $Z$  production and  $Z$ +jets, probing quark electroweak couplings and dipole interactions [7–10].

Despite this progress,  $Z$ -boson decays into mixed leptonic–hadronic final states remain relatively unexplored in the SMEFT context. Such channels are sensitive to a distinct set of operators, in particular four-fermion contact interactions involving both leptons and quarks, as well as flavor-dependent modifications of  $Z$ –fermion couplings [11]. Among these, the decay  $Z \rightarrow \mu\mu b\bar{b}$  is of special interest. The presence of bottom quarks enhances sensitivity to operators coupling to the third quark generation, while the dimuon final state allows for precise reconstruction of the leptonic kinematics. At the same time, the analysis poses experimental challenges due to sizable QCD backgrounds and the reliance on heavy-flavor tagging [12, 13].

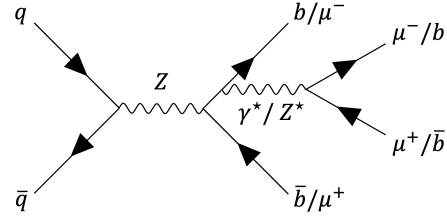


FIG. 1: Representative Feynman diagram contributing to the process  $Z \rightarrow \mu\mu b\bar{b}$  in the Standard Model, where the four-body final state arises from final-state radiation of an off-shell  $Z^*/\gamma^*$ .

The diagram shown in FIG. 1 illustrates the characteristic topology of the  $Z \rightarrow \mu\mu b\bar{b}$  decay in the Standard Model, where the four-body final state arises predominantly from final-state radiation of an off-shell electroweak gauge boson. Compared to two-body  $Z$  decays, this topology probes a richer kinematic structure and allows access to contact interactions that are absent at leading order in simpler final states. In the SMEFT framework, this process is particularly sensitive to four-fermion operators involving muons and bottom quarks, which generate direct  $\mu\mu b\bar{b}$  interactions at tree level. Such contributions interfere with the SM amplitudes mediated by off-shell  $Z^*/\gamma^*$  exchange, leading to characteristic deviations in both the total rate and differential distributions. As a result, the  $Z \rightarrow \mu\mu b\bar{b}$  channel provides a complementary, process-specific probe of lepton–quark operator structures that are only weakly constrained by inclusive  $Z$  observables or purely leptonic decay modes.

In this work, we perform a dedicated SMEFT analysis of the decay  $Z \rightarrow \mu\mu b\bar{b}$  and derive constraints on dimension-six operators contributing to this process. We focus on operators that induce four-fermion interactions of the  $\ell\ell b\bar{b}$  type and on operators that modify the  $Z$  couplings to leptons and bottom quarks. Signal and background processes are simulated using state-of-the-art

\* wangzijian@stu.pku.edu.cn

Monte Carlo tools, and detector-level effects are included [14–16]. Limits on the WCs are obtained from differential distributions using a profile likelihood approach [17].

This study provides a complementary probe of new physics effects in the  $Z$ -boson sector, extending existing SMEFT constraints beyond purely leptonic final states. It demonstrates the potential of mixed leptonic–hadronic  $Z$  decays to access operator directions that are weakly constrained by current analyses and motivates their inclusion in future global SMEFT fits [18].

## II. EFFECTIVE FIELD THEORY DESCRIPTION

In the absence of direct evidence for new resonances, the effects of physics beyond the Standard Model (SM) can be systematically described using an effective field theory approach [4–6]. Its low-energy effects can be encoded in higher-dimensional operators constructed from SM fields and respecting the SM gauge symmetries.

Within the SMEFT framework, the Lagrangian is organized as an expansion in inverse powers of the new physics scale  $\Lambda$ ,

$$\mathcal{L}_{\text{SMEFT}} = \mathcal{L}_{\text{SM}} + \sum_i \frac{C_i}{\Lambda^2} \mathcal{O}_i + \mathcal{O}\left(\frac{1}{\Lambda^4}\right), \quad (1)$$

where  $\mathcal{O}_i$  are dimension-six operators and  $C_i$  the corresponding WCs [10, 11]. In this work, we truncate the expansion at dimension six contributions [19, 20].

The decay  $Z \rightarrow \mu b\bar{b}$  receives contributions from several classes of dimension-six operators. First, four-fermion operators involving leptons and bottom quarks generate direct contact interactions contributing to the four-body final state at tree level [7, 8]. Schematically, such operators can be written as  $(\bar{\ell}\Gamma\ell)(\bar{q}\Gamma q)$  and induce amplitudes that interfere with the SM contributions mediated by off-shell electroweak bosons.

Second, operators that modify the couplings of the  $Z$  boson to fermions lead to indirect contributions to the decay process. After electroweak symmetry breaking, these operators generate shifts in the effective  $Z$ –lepton and  $Z$ –quark couplings, which affect both the production and decay of the  $Z$  boson [18, 21]. These effects propagate into the  $Z \rightarrow \mu b\bar{b}$  final state through the modified electroweak vertices.

In the numerical analysis, we select a set of six dimension-six operators that contribute to this decay channel and study their impact individually. The operators are implemented using the `SMEFTsim_general_MwScheme_UFO` model [6, 22], which is compatible with `MadGraph5_aMC@NLO` [14] and allows event generation and reweighting at leading order in a consistent electroweak input scheme.

In this analysis, we retain both the interference and quadratic terms in the WCs when evaluating SMEFT effects [7]. The dependence of physical observables on

a given WC is therefore parameterized by a quadratic function, which can be efficiently determined using the reweighting technique [14]. This approach allows us to explore the parameter space of the WCs without generating independent event samples for each point.

The validity of the SMEFT expansion relies on the assumption that the typical energy scale of the process remains below the cutoff scale  $\Lambda$  [10, 19]. In practice, the absence of events with extremely large  $m_{\mu b\bar{b}}$  or jet transverse momenta indicates that the analysis is dominated by energy scales safely below the assumed new physics cutoff.

## III. EVENT GENERATION AND SIMULATION

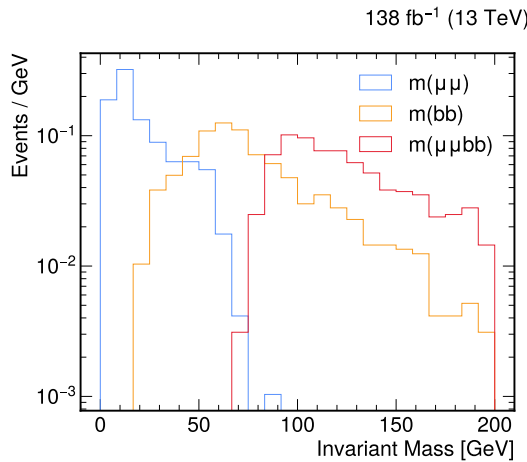
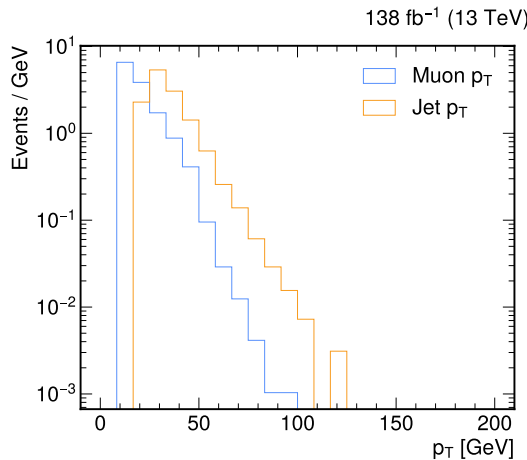
All processes are generated at leading order using `MadGraph5_aMC@NLO`, followed by parton showering and hadronization with `Pythia8` [15]. Detector-level effects are simulated using `Delphes` [16] with an CMS-like detector configuration. Unless stated otherwise, proton–proton collisions at a center-of-mass energy of  $\sqrt{s} = 13$  TeV are assumed throughout this analysis.

The signal process considered in this work is the four-body decay of the  $Z$  boson into a dimuon pair and a bottom–antibottom quark pair:  $Z \rightarrow \mu b\bar{b}$ . At leading order, the four-body final state arises predominantly from final-state radiation or off-shell electroweak boson exchange [7]. Representative Feynman diagrams contributing to the signal process are shown in Fig. 1.

Signal events are generated at parton level using `MadGraph5_aMC@NLO`. Basic generator-level cuts are applied to ensure numerical stability and reflect the kinematic acceptance of the detector:  $p_T^\ell > 10$  GeV,  $|\eta^\ell| < 2.5$  for charged leptons, and  $p_T^q > 10$  GeV,  $|\eta^q| < 2.5$  for quarks. The resulting leading-order cross section for the signal process is  $\sigma(Z \rightarrow \mu^+ \mu^- b\bar{b}) = 0.750$  fb, where the quoted uncertainty corresponds to the Monte Carlo integration error.

The reconstructed kinematic distributions shown in Fig. 2 provide an important validation of the signal modeling after detector effects are taken into account. In Fig. 2a, the invariant mass distribution of the  $b\bar{b}$  system is considerably broader than that of dimuon system, as expected from jet energy resolution effects and QCD radiation. Nevertheless, the combined four-body invariant mass  $m_{\mu b\bar{b}}$  displays a clear enhancement around  $m_Z$ , indicating that the signal topology can be reliably reconstructed at detector level despite the presence of hadronic final states.

Fig. 2b shows the transverse momentum spectra of the reconstructed muons and jets. The muon  $p_T$  distribution is relatively soft, characteristic of a  $Z$ -boson decay, while the jet  $p_T$  spectrum features a longer tail driven by QCD dynamics. The typical energy scales involved remain well below the assumed SMEFT cutoff, supporting the consistency of the SMEFT interpretation within the selected phase space.

(a) Invariant mass distributions of  $\mu\mu$ ,  $bb$ , and  $\mu\mu bb$ .

(b) Transverse momentum distributions of muons and jets.

FIG. 2: Detector-level kinematic distributions for the process  $Z \rightarrow \mu\mu bb$  obtained from **Delphes** simulation.

The dominant background arises from top-quark pair production  $pp \rightarrow t\bar{t}$ , with both top quarks decaying semileptonically,  $t \rightarrow b\mu^+\nu_\mu$  and  $\bar{t} \rightarrow b\mu^-\bar{\nu}_\mu$  [14, 15]. Due to its large production cross section, this process remains a significant background even after event selection.

Additional backgrounds include diboson production, such as  $pp \rightarrow ZZ$ ,  $Z \rightarrow \mu\mu$ ,  $Z \rightarrow bb$  as well as associated production of a  $Z$  boson with a Higgs boson:  $pp \rightarrow ZH$ ,  $Z \rightarrow \mu^+\mu^-$ ,  $H \rightarrow b\bar{b}$ . Although their cross sections are smaller than that of  $t\bar{t}$  production, these processes closely resemble the signal topology and are therefore included explicitly [14, 16].

The Drell-Yan production of a  $Z$  boson in association with jets:  $pp \rightarrow Z + \text{jets}$ , constitutes another important background due to its very large cross section. Events with light-flavor jets can enter the signal region through jet misidentification, while events with heavy-flavor jets provide an irreducible background. To model this back-

ground accurately, samples with up to two additional jets at matrix-element level are generated and merged with the parton shower using the MLM matching scheme [23, 24].

Subleading backgrounds from electroweak processes involving photons are also considered, including  $Z\gamma$ ,  $\gamma\gamma$ , and mixed  $\gamma Z$  production, where the photon converts into a fermion pair.

A summary of all signal and background processes and their corresponding leading-order cross sections is given in TABLE I.

Process	Cross section [pb]
$pp \rightarrow Z$ , $Z \rightarrow \mu^+\mu^- b\bar{b}$	$7.50 \times 10^{-4}$
$pp \rightarrow t\bar{t}$ , $t \rightarrow b\mu^+\nu_\mu$ , $\bar{t} \rightarrow b\mu^-\bar{\nu}_\mu$	4.38
$pp \rightarrow ZZ$ , $Z \rightarrow \mu^+\mu^-$ , $Z \rightarrow b\bar{b}$	$5.54 \times 10^{-2}$
$pp \rightarrow Z + \text{jets}$ (0, 1, 2)	$9.33 \times 10^2$
$pp \rightarrow ZH$ , $Z \rightarrow \mu^+\mu^-$ , $H \rightarrow b\bar{b}$	$1.03 \times 10^{-2}$
$pp \rightarrow Z\gamma$ , $\gamma \rightarrow b\bar{b}$	$5.54 \times 10^{-3}$
$pp \rightarrow \gamma\gamma$ , $\gamma \rightarrow \mu^+\mu^-$ , $\gamma \rightarrow b\bar{b}$	$6.70 \times 10^{-5}$

TABLE I: Leading-order cross sections for the signal and background processes considered in this analysis. The quoted uncertainties correspond to Monte Carlo integration errors. The merged  $Z + \text{jets}$  sample, combining matrix-element calculations with up to two additional jets, is used in the final analysis, while the individual samples are shown for reference.

All generated parton-level events are passed to **Pythia8** for parton showering and hadronization. For the  $Z + \text{jets}$  background, matrix-element calculations with up to two additional jets are merged with the parton shower using the MLM matching scheme [23, 24]. This procedure avoids double counting between matrix-element and parton-shower emissions and provides a more reliable description of multi-jet final states.

Detector effects are simulated with **Delphes**, using a CMS-like detector configuration. Jets are identified as  $b$ -jets using the built-in  $b$ -tagging algorithm, and a fixed working point corresponding to a discriminator threshold of  $\text{BTag} > 0.5$  is applied. This working point yields an average  $b$ -tagging efficiency of approximately 70% for true  $b$ -jets, with mis-tag rates of about 10% for charm jets and 1% for light-flavor jets, consistent with typical CMS performance [25]. The requirement of two  $b$ -tagged jets significantly suppresses backgrounds from light-flavor and charm jet production, in particular from  $Z + \text{jets}$  events.

#### IV. EVENT RECONSTRUCTION AND SELECTION STRATEGY

Events are reconstructed using the detector-level objects provided by **Delphes**. Muon candidates are reconstructed within the pseudorapidity range  $|\eta| < 2.5$ , corresponding to the coverage of the central tracking system and muon chambers in LHC experiments [26, 27]. Jets are reconstructed using the anti- $k_T$  algorithm with a radius parameter  $R = 0.4$  [28].

Bottom-quark jets are identified using the  $b$ -tagging information stored in the **Delphes** output [16, 29]. A jet is considered a  $b$ -jet if its  $b$ -tag discriminator exceeds a threshold of 0.5, corresponding to a typical medium working point used in CMS analyses. Jets are identified as  $b$ -jets using the  $b$ -tagging discriminator provided by **Delphes**, adopting a medium working point.

To emulate the trigger requirements of LHC experiments, events are required to satisfy at least one of the muon-based trigger conditions listed in TABLE II. These triggers are motivated by standard CMS single- and double-muon triggers used in Run II analyses [30]. The single-muon trigger ensures high efficiency for events containing a high- $p_T$  muon, while the di-muon trigger retains sensitivity to events in which both muons have moderate transverse momenta. Only isolated muons are considered for trigger selection to suppress backgrounds from heavy-flavor decays and hadronic activity.

Trigger requirement	Threshold [GeV]
Single-muon trigger	$p_T(\mu) > 25$
Double-muon trigger (leading)	$p_T(\mu_1) > 18$
Double-muon trigger (subleading)	$p_T(\mu_2) > 7$

TABLE II: Muon trigger requirements used in the analysis. Only isolated muons are considered for trigger selection.

Events passing the trigger requirements are subjected to a set of preselection criteria designed to suppress reducible backgrounds while maintaining high signal efficiency. The preselection cuts are summarized in TABLE III.

At least two muon candidates are required per event. The subleading muon is required to satisfy  $p_T > 10$  GeV to ensure reliable reconstruction and identification efficiency. Muon isolation is imposed by requiring a minimum separation  $\Delta R(\mu, \text{jet}) > 0.4$  between each selected muon and any reconstructed jet [28]. This reduces backgrounds from semileptonic heavy-flavor decays.

To suppress backgrounds containing genuine missing transverse energy, such as top-quark pair production, events are required to have  $\text{MET} < 30$  GeV. This exploits the absence of neutrinos in the signal process  $Z \rightarrow \mu\mu bb$ .

Events are required to contain at least two reconstructed jets with  $p_T > 25$  GeV, among which at least two must be identified as  $b$ -jets. This reflects the expected presence of a  $b\bar{b}$  pair in the signal final state and significantly suppresses backgrounds from  $Z +$  light-jets production.

Angular separation requirements are imposed to ensure well-resolved final-state objects. In particular, the separation between the two selected  $b$ -jets must satisfy  $\Delta R(b, b) > 0.4$ , and the separation between the two leading muons must satisfy  $\Delta R(\mu, \mu) > 0.4$ . Additionally, all muon- $b$ -jet pairs must satisfy  $\Delta R(\mu, b) > 0.4$  [28]. These requirements reduce contamination from collinear final-state radiation and overlapping reconstruction effects.

Selection	Requirement
Number of muons	$\geq 2$
Muon $p_T$ (subleading)	$> 10$ GeV
Muon isolation	$\Delta R(\mu, \text{jet}) > 0.4$
Missing transverse energy	$\text{MET} < 30$ GeV
Number of jets	$\geq 2$
Jet $p_T$	$> 25$ GeV
$b$ -tagging	$\geq 2$ $b$ -jets
$\Delta R(b, b)$	$> 0.4$
$\Delta R(\mu, \mu)$	$> 0.4$
$\Delta R(\mu, b)$	$> 0.4$

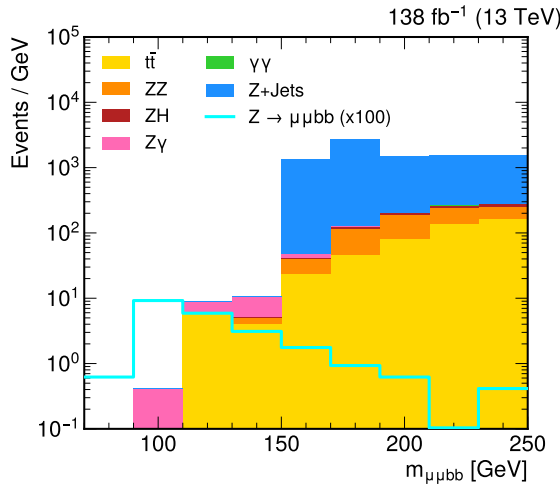
TABLE III: Summary of event selection criteria applied in the analysis.

The selection criteria are designed to preserve the characteristic kinematics of the  $Z \rightarrow \mu\mu bb$  decay while suppressing backgrounds with genuine missing energy or misidentified heavy-flavor jets. For events passing all selection requirements, the invariant mass of the  $\mu\mu bb$  system is reconstructed using the four-momenta of the two leading isolated muons and the two selected  $b$ -jets. The reconstructed invariant mass  $m_{\mu\mu bb}$ , serves as the primary observable for signal extraction and the subsequent SMEFT analysis [7].

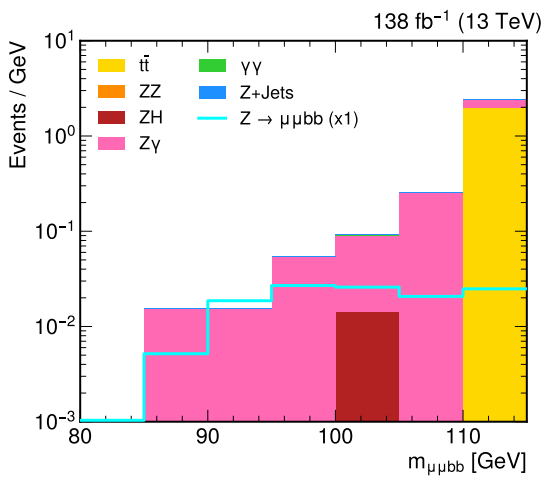
The signal region is defined as  $80 \text{ GeV} < m_{\mu\mu bb} < 115 \text{ GeV}$ , centered around the  $Z$  boson mass. This window retains the majority of the signal while efficiently suppressing non-resonant backgrounds. This window is chosen to maximize sensitivity to SMEFT-induced rate deviations while minimizing contamination from non-resonant backgrounds.

FIG. 3 compares the reconstructed invariant mass distributions of the  $\mu\mu bb$  system for the signal and the dominant background processes after the full event selection. In FIG. 3a, the distribution is shown over a wide mass range from 70 to 250 GeV, with the signal contribution scaled by a factor of 100 for visibility. Over this range,

the spectrum is dominated by the  $Z + \text{jets}$  and  $t\bar{t}$  backgrounds, reflecting their large production cross sections.



(a) Invariant mass distributions in the (70, 250) GeV range, full spectrum with signal scaled by 100 for visibility.



(b) Invariant mass distributions in the (80, 115) GeV range, focusing on the signal region.

FIG. 3: Detector-level invariant mass distributions for  $\mu\mu bb$  from various processes, obtained from `Delphes` simulation. The first panel shows the full mass spectrum with the signal scaled for better visibility, while the second panel zooms into the signal region.

FIG. 3b focuses on the signal region defined by  $80 < m_{\mu\mu bb} < 115$  GeV, which is centered around the  $Z$  boson mass. In this window, the signal contribution becomes clearly distinguishable, while the  $t\bar{t}$  background is strongly suppressed by the missing transverse energy requirement. The remaining backgrounds, including  $Z\Lambda$  and  $ZH$  production, exhibit similar kinematic features but are subleading in rate. This demonstrates that the chosen invariant mass window provides an optimal bal-

ance between signal efficiency and background rejection, forming a robust basis for the subsequent SMEFT analysis. The clear localization of the signal contribution within the  $Z$ -mass window demonstrates that the invariant mass  $m_{\mu\mu bb}$  provides a powerful discriminator for isolating SMEFT effects in this channel. This observable is therefore chosen as the primary input for the subsequent reweighting and limit-setting procedure.

## V. SMEFT REWEIGHTING AND CONSTRAINING

The impact of dimension-six operators on the process  $Z \rightarrow \mu\mu bb$  is evaluated within the SMEFT framework using an event reweighting technique [31, 32]. In this approach, the effect of each WC on the cross section and kinematic distributions is obtained by reweighting SM Monte Carlo events. The total event weight includes the Standard Model contribution as well as linear and quadratic corrections from dimension-six operators, allowing an efficient exploration of the WCs parameter space without regenerating new event samples.

SMEFT effects are incorporated using the `SMEFTsim_general_MwScheme_UFO` model from the `SMEFTsim` 3.0 framework [6, 22], which provides a complete and gauge-invariant implementation of dimension-six operators in the  $M_W$  input scheme. The  $M_W$  scheme is adopted to consistently account for electroweak input-parameter shifts induced by dimension-six operators. For each generated event, a set of precomputed weights corresponding to different values of  $\theta$  is stored and propagated through parton showering, hadronization, and detector simulation, ensuring a consistent treatment of SM and SMEFT contributions [15, 16].

After applying the full event selection, the expected number of signal events is expressed as a quadratic function of the WCs parameter  $\theta \equiv C_i/\Lambda^2$ ,

$$N(\theta) = c + b\theta + a\theta^2, \quad (2)$$

where  $c$  denotes the Standard Model (SM) expectation,  $b$  corresponds to the interference between the SM and dimension-six amplitudes, and  $a$  encodes the pure quadratic SMEFT contribution [7]. The coefficients  $a$ ,  $b$ , and  $c$  are determined by fitting the event yields obtained from reweighted samples generated at several fixed values of  $\theta$ .

Constraints on the WCs are derived using a likelihood-based statistical approach [17]. An Asimov dataset is constructed by assuming the observed number of events to be equal to the SM prediction,  $N_{\text{obs}} = N_{\text{SM}} \equiv c$ . The Poisson likelihood function is then given by

$$\mathcal{L}(\theta) = \frac{[N(\theta)]^{N_{\text{obs}}} e^{-N(\theta)}}{N_{\text{obs}}!}. \quad (3)$$

The test statistic is defined as the likelihood ratio

$$q(\theta) = -2 \ln \frac{\mathcal{L}(\theta)}{\mathcal{L}(0)} = 2 \left[ N(\theta) \ln \frac{N(\theta)}{N_{\text{SM}}} + N_{\text{SM}} - N(\theta) \right], \quad (4)$$

which, under the assumptions of Wilks' theorem, follows a  $\chi^2$  distribution with one degree of freedom [33]. The 95% confidence level (C.L.) interval on  $\theta$  is obtained by requiring  $q(\theta) = 3.84$ .

The resulting constraint is quoted both in terms of the WCs,  $\theta_{95} = C_i/\Lambda^2$ , and in terms of the relative deviation of the expected event yield with respect to the SM prediction,

$$R_{95} \equiv \frac{N(\theta_{95})}{N_{\text{SM}}}. \quad (5)$$

This procedure is applied independently to each dimension-six operator, with all other WCs set to zero, providing a measure of the sensitivity of the  $Z \rightarrow \mu\mu bb$  channel to physics beyond the Standard Model within the SMEFT framework. In this analysis, a flavor-specific setup is adopted, in which the WCs are defined for individual fermion generations. In particular, operators involving second-generation leptons ( $\ell_2$ ) and third-generation quarks ( $q_3$ ) are considered explicitly. This choice allows a direct probe of flavor-resolved SMEFT effects in the  $Z \rightarrow \mu\mu bb$  final state, beyond the flavor-universal assumptions commonly employed in global SMEFT fits.

FIG. 4 shows the dependence of the expected event yield in the signal region on the WCs of the six dimension-six operators considered in this analysis. For each operator, the ratio of the SMEFT prediction to the SM expectation is fitted with a quadratic function, reflecting the structure of the squared matrix element, which includes both interference and pure SMEFT contributions.

The observed quadratic behavior confirms the validity of the reweighting procedure and illustrates the relative importance of linear and quadratic terms for different operator classes. Operators modifying the  $Z$ -fermion couplings exhibit sizable interference with the SM amplitude, leading to asymmetric constraints around the SM point. In contrast, certain four-fermion operators show a more symmetric dependence, indicating a dominant contribution from the quadratic term. This behavior highlights the particular sensitivity of this channel to four-fermion operators involving bottom quarks.

The resulting 95% C.L. intervals on the WCs obtained from this procedure are summarized in Table IV. The constraints obtained in this analysis can be compared with existing global SMEFT interpretations from the CMS Collaboration [34]. In the CMS combined analysis, stringent limits are reported on operators that modify the couplings of electroweak gauge bosons to fermions, such as  $C_{H\ell}^{(1,3)}$  and  $C_{Hq}^{(1,3)}$ , under flavor-universal or top-specific assumptions. These limits, typically at the level of  $\mathcal{O}(10^{-3})$ – $\mathcal{O}(10^{-2})$  TeV $^{-2}$  at 95% C.L., are primarily

driven by electroweak precision observables, Higgs measurements, and top-quark processes.

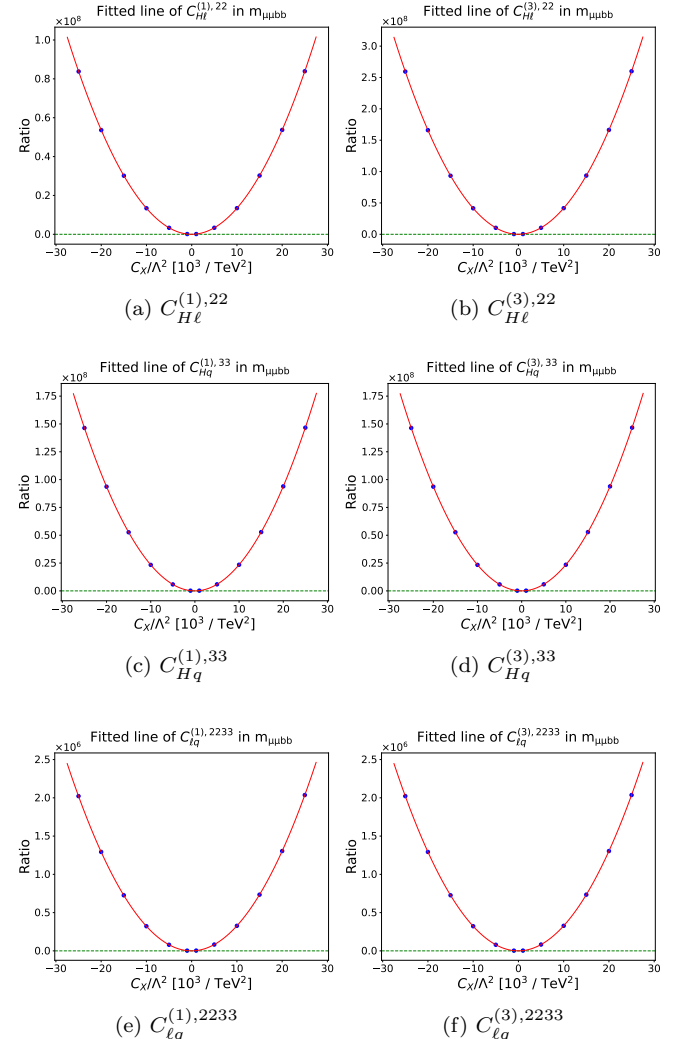


FIG. 4: Quadratic SMEFT fits for the six operators under study. Each panel shows the fitted yield as a function of the WCs for the corresponding operator, with points representing simulated events and the red line indicating the quadratic fit. The legend shows the operator name following the SMEFTsim 3.0 conventions.

In contrast, the present analysis focuses on flavor-resolved WCs involving second-generation leptons and third-generation quarks. The constraints derived for  $C_{H\ell}^{(1,3),22}$  and  $C_{Hq}^{(1,3),33}$  can therefore be directly interpreted as channel-specific probes of the same operator classes considered in the CMS global fit, but obtained from a single decay mode and a cut-based analysis.

The constraints obtained here for  $C_{H\ell}^{(1,3),22}$  and  $C_{Hq}^{(1,3),33}$  are found to be of the same order of magnitude as those from the CMS global fit, despite being derived from a single decay channel and a cut-based analysis. For the four-

fermion operators  $C_{\ell q}^{(1,3),2233}$ , which describe contact interactions between second-generation leptons and third-generation quarks, no direct constraints are currently available from global SMEFT fits, where such flavor-specific four-fermion operators are typically neglected or marginalized. The limits presented in this work therefore provide the first process-specific constraints on these operators from  $Z$ -boson decays. These results demonstrate the unique sensitivity of the  $Z \rightarrow \mu\mu bb$  final state to four-fermion interactions involving bottom quarks, which are difficult to access in inclusive or flavor-universal analyses. The projected HL-LHC dataset, with an integrated luminosity of  $3000 \text{ fb}^{-1}$ , further improves the constraints and providing a flavor-resolved probe complementary to existing CMS global analyses. In particular, the HL-LHC projections confirm the unique potential of the  $Z \rightarrow \mu\mu bb$  channel to constrain four-fermion interactions involving bottom quarks.

$C$	$138 \text{ fb}^{-1}$	$3000 \text{ fb}^{-1}$
$C_{\ell q}^{(1),2233}$	$[-0.023, 0.014]$	$[-0.005, 0.003]$
$C_{\ell q}^{(3),2233}$	$[-0.023, 0.014]$	$[-0.005, 0.003]$
$C_{Hq}^{(1),33}$	$[-0.029, 0.026]$	$[-0.006, 0.006]$
$C_{Hq}^{(3),33}$	$[-0.030, 0.026]$	$[-0.006, 0.006]$
$C_{H\ell}^{(1),22}$	$[-0.025, 0.009]$	$[-0.005, 0.002]$
$C_{H\ell}^{(3),22}$	$[-0.028, 0.025]$	$[-0.006, 0.005]$

TABLE IV: 95% C.L. allowed regions for  $C/\Lambda^2$  [TeV $^{-2}$ ].

## VI. CONCLUSIONS

In this work, we have presented a phenomenological study of the  $Z \rightarrow \mu\mu bb$  final state as a probe of physics beyond the Standard Model within the framework of the Standard Model Effective Field Theory. The analysis is entirely based on Monte Carlo simulations and aims at assessing the sensitivity of this channel to a selected set of dimension-six SMEFT operators.

Signal and relevant background processes were generated at leading order using `MadGraph5_aMC@NLO`, followed by parton showering and hadronization with `Pythia`, and a fast detector simulation with `Delphes`. A realistic event selection strategy was implemented, including

trigger requirements, lepton isolation,  $b$ -jet identification, and kinematic separation cuts. After event reconstruction, the invariant mass distribution of the  $\mu\mu bb$  system, together with transverse momentum spectra of the final-state objects, was used to validate the signal modeling and background suppression.

To quantify possible deviations from the Standard Model, we employed the SMEFT reweighting technique using a UFO implementation of dimension-six operators. For each operator under consideration, event weights corresponding to multiple values of the WC were extracted at the generator level and propagated through the full analysis chain. The total event yield after selection was shown to follow a quadratic dependence on the WC, reflecting the interference and pure SMEFT contributions to the cross section.

A likelihood-based statistical analysis was performed by constructing a test statistic based on the expected event yields. Assuming the Standard Model prediction as the null hypothesis, we derived 95% confidence level constraints on the WCs by identifying the parameter values corresponding to the critical value of the test statistic. This procedure provides a transparent and robust estimate of the sensitivity of the  $\mu\mu bb$  channel to SMEFT effects, in the absence of experimental systematic uncertainties associated with real data.

The results demonstrate that the  $Z \rightarrow \mu\mu bb$  final state constitutes a viable and complementary probe of electroweak and Higgs-related effective operators. Although the present study is limited to leading-order simulations and an inclusive cut-based analysis, it establishes a solid baseline for future improvements. Possible extensions include the incorporation of higher-order corrections, a differential shape analysis, the inclusion of systematic uncertainties, and a global fit combining multiple final states.

Overall, this work highlights the potential of precision studies of multi-body  $Z$ -boson decay final states within the SMEFT framework and demonstrates that mixed leptonic–hadronic channels can provide unique and complementary information on flavor-resolved new physics interactions.

## ACKNOWLEDGMENTS

This work is supported in part by the National Natural Science Foundation of China under Grants No. 12325504.

---

[1] ALEPH Collaboration. Precision electroweak measurements on the  $z$  resonance. *Phys. Rept.*, 427:257–454, 2006.

[2] ATLAS Collaboration. Measurement of the  $z$  boson production cross section in  $pp$  collisions at  $\sqrt{s} = 13$  tev with the atlas detector. *JHEP*, 09:145, 2016.

[3] CMS Collaboration. Measurement of differential  $z$  boson production cross sections in proton-proton collisions at  $\sqrt{s} = 13$  tev. *JHEP*, 12:061, 2019.

[4] W. Buchmuller and D. Wyler. Effective lagrangian analysis of new interactions and flavor conservation. *Nucl. Phys. B*, 268:621–653, 1986.

[5] B. Grzadkowski, M. Iskrzynski, M. Misiak, and J. Rosiek. Dimension-six terms in the standard model lagrangian.

*JHEP*, 10:085, 2010.

[6] I. Brivio and M. Trott. The standard model as an effective field theory. *Phys. Rept.*, 793:1–98, 2019.

[7] R. Boughezal, B. Fuks, B. D. Pecjak, and C. Zhang. Probing the smeft in  $z \rightarrow 4\ell$  decays at the lhc. *JHEP*, 06:131, 2020.

[8] R. Gauld and B. D. Pecjak. Four-lepton production at the lhc and smeft constraints. *JHEP*, 07:090, 2020.

[9] R. Gauld et al. Smeft interpretations of inclusive  $z$ -jets production. *JHEP*, 01:145, 2024.

[10] A. Falkowski and F. Riva. Model-independent precision constraints on dimension-6 operators. *JHEP*, 02:039, 2015.

[11] L. Berthier and M. Trott. Consistent constraints on the standard model effective field theory. *JHEP*, 02:069, 2016.

[12] CMS Collaboration. Measurement of  $z$ +b-jet cross sections at  $\sqrt{s} = 13$  tev. *Eur. Phys. J. C*, 79:368, 2019.

[13] ATLAS Collaboration. Measurements of  $z$  boson production in association with  $b$ -jets in pp collisions at 13 tev. *Phys. Lett. B*, 789:347–366, 2019.

[14] J. Alwall, R. Frederix, S. Frixione, V. Hirschi, F. Maltoni, O. Mattelaer, H.-S. Shao, T. Stelzer, P. Torrielli, and M. Zaro. The automated computation of tree-level and next-to-leading order differential cross sections, and their matching to parton shower simulations. *JHEP*, 07:079, 2014.

[15] T. Sjöstrand, S. Ask, J. R. Christiansen, R. Corke, N. De-sai, P. Ilten, S. Mrenna, S. Prestel, C. O. Rasmussen, and P. Skands. An introduction to pythia 8.2. *Comput. Phys. Commun.*, 191:159–177, 2015.

[16] J. de Favereau et al. Delphes 3, a modular framework for fast simulation of a generic collider experiment. *JHEP*, 02:057, 2014.

[17] G. Cowan, K. Cranmer, E. Gross, and O. Vitells. Asymptotic formulae for likelihood-based tests of new physics. *Eur. Phys. J. C*, 71:1554, 2011.

[18] J. Ellis, C. W. Murphy, V. Sanz, and T. You. Updated global smeft fit to higgs, diboson and electroweak data. *JHEP*, 06:146, 2018.

[19] J. Elias-Miro, J. R. Espinosa, E. Masso, and A. Pomarol. Higgs windows to new physics through dimension-6 operators. *JHEP*, 11:066, 2013.

[20] T. Corbett, O. J. P. Eboli, J. Gonzalez-Fraile, and M. C. Gonzalez-Garcia. Determining triple gauge boson couplings from higgs data. *Phys. Rev. Lett.*, 111:011801, 2013.

[21] J. de Blas and et al. The global smeft fit. *JHEP*, 12:135, 2018.

[22] Ilaria Brivio. Smeftsim 3.0 — a practical guide. *Journal of High Energy Physics*, 2021(4), April 2021.

[23] M. L. Mangano, M. Moretti, F. Piccinini, R. Pittau, and A. D. Polosa. Alpgen, a generator for hard multiparton processes in hadronic collisions. *JHEP*, 07:001, 2003.

[24] J. Alwall and et al. Comparative study of various algorithms for the merging of parton showers and matrix elements in hadronic collisions. *Eur. Phys. J. C*, 53:473–500, 2008.

[25] The CMS collaboration. Identification of b-quark jets with the cms experiment. *Journal of Instrumentation*, 8(04):P04013–P04013, April 2013.

[26] S. Chatrchyan and et al. The cms experiment at the cern lhc. *JINST*, 3:S08004, 2008.

[27] G. Aad and et al. The atlas experiment at the cern large hadron collider. *JINST*, 3:S08003, 2008.

[28] M. Cacciari, G. P. Salam, and G. Soyez. The anti- $k_t$  jet clustering algorithm. *JHEP*, 04:063, 2008.

[29] CMS Collaboration. Identification of b-quark jets with the cms experiment. *JINST*, 8:P04013, 2013.

[30] CMS Collaboration. Performance of the cms muon detector and muon reconstruction with proton-proton collisions at  $\sqrt{s} = 13$  tev. *JINST*, 13:P06015, 2018.

[31] E. Conte, B. Fuks, and G. Serret. Madanalysis 5, a user-friendly framework for collider phenomenology. *Comput. Phys. Commun.*, 184:222–256, 2013.

[32] A. Alloul, N. D. Christensen, C. Degrande, C. Duhr, and B. Fuks. Feynrules 2.0 - a complete toolbox for tree-level phenomenology. *Comput. Phys. Commun.*, 185:2250–2300, 2014.

[33] S. S. Wilks. The large-sample distribution of the likelihood ratio for testing composite hypotheses. *Annals Math. Statist.*, 9:60–62, 1938.

[34] CMS Collaboration. Combined effective field theory interpretation of higgs boson, electroweak vector boson, top quark, and multi-jet measurements, 2025.